# Noise-based ballistic wave passive seismic monitoring - Part 2: surface waves

Aurélien Mordret, Roméo Courbis, Florent Brenguier, Malgorzata Chmiel, Stéphane Garambois, Shujuan Mao, Pierre Boué, Xander Campman, Thomas Lecocq, Wim Van der veen, et al.

submitted to *Geophys. J. Int.*

# Noise-based Ballistic Wave Passive Seismic Monitoring – Part 2: Surface Waves

Aurélien Mordret[1⋆], Roméo Courbis[2–3], Florent Brenguier[2], Małgorzata Chmiel[2–3], Stéphane Garambois[2], Shujuan Mao[1], Pierre Boué[2], Xander Campman[4], Thomas Lecocq[5], Wim Van der Veen[6] and Dan Hollis[3]

[1]*Department of Earth, Atmospheric and Planetary Sciences, Massachusetts Institute of Technology (MIT), Cambridge, Massachusetts, USA*

[2]*Université Grenoble Alpes, Univ. Savoie Mont Blanc, CNRS, IRD, IFSTTAR, ISTerre, UMR 5275, 38000 Grenoble, France*

[3]*Sisprobe, Meylan, 38240, France*

[4]*Shell Global Solutions International BV, Amsterdam, the Netherlands*

[5]*Royal Observatory of Belgium - Seismology, Avenue Circulaire, 3, BE-1180 Brussels, Belgium*

[6]*Nederlandse Aardolie Maatschappij.*

2 December 2019

**SUMMARY**

We develop a new method to monitor and locate seismic velocity changes in the subsurface using seismic noise interferometry. Contrary to most ambient noise monitoring techniques, we use the ballistic Rayleigh waves computed from 30 days records on a dense nodal array located above the Groningen gas field (the Netherlands), instead of their coda waves. We infer the daily relative phase velocity dispersion changes as a function of frequency and propagation distance with a cross-wavelet transform processing. Assuming a one-dimensional velocity change within the medium, the induced ballistic Rayleigh wave phase shift exhibits a linear trend as a function of the propagation distance. Measuring this trend for the fundamental mode and the first overtone of the Rayleigh waves for frequencies between 0.5 and 1.1 Hz enables us to invert for shear-wave daily velocity changes in the first 1.5 km of the subsurface. The observed deep velocity changes ($\pm$ 1.5%) are difficult to interpret given the environmental factors information available. Most of the observed shallow changes seem associated with effective pressure variations. We observe a reduction of shear-wave velocity (-0.2%) at the time of a large rain event accompanied by a strong decrease in atmospheric pressure loading, followed by a migration at depth of the velocity decrease. Combined with P-wave velocity changes observations from a companion paper, we interpret the changes as caused by the diffusion of effective pressure variations at depth. As a new method, noise-based ballistic wave passive monitoring could be used on several dynamic (hydro-)geological targets and in particular, it could be used to estimate hydrological parameters such as the hydraulic conductivity and diffusivity.

**Key words:** Seismic tomography; Seismic interferometry; Wave scattering and diffraction; Wave propagation; Surface waves and free oscillations

## 1 INTRODUCTION

Ambient seismic noise interferometry (e.g., Shapiro & Campillo 2004; Wapenaar et al. 2010) via Coda Wave Interferometry (CWI, e.g., Snieder et al. 2002; Sens-Schönfelder & Wegler 2006; Brenguier et al. 2008b) has become the most efficient way to probe continuous temporal changes of the elastic properties of the crust. It has successfully been applied to volcano monitoring during pre- and co-eruptive stages (Brenguier et al. 2008b; Mordret et al. 2010; Yukutake et al. 2016) or inter-eruptive periods (e.g., Sens-Schönfelder & Wegler 2006; Rivet et al. 2014; Donaldson et al. 2017). It has also been used to monitor the response of the crust to large earthquakes (e.g., Wegler & Sens-Schönfelder 2007; Brenguier et al. 2008a; Minato et al. 2012; Brenguier et al. 2014) or slow-slip events (Rivet et al. 2011). More recently, it has contributed to the fast emergence of environmental seismology applications (Mainsant et al. 2012; Gassenmeier et al. 2014; Larose et al. 2015; Mordret et al. 2016; Lecocq et al. 2017; Clements & Denolle 2018; Mao et al. 2019a;

⋆ Corresponding author, mordret@mit.edu

Fores et al. 2018) and passive seismic monitoring of civil engineering structures (Nakata & Snieder 2013; Salvermoser et al. 2015; Planès et al. 2015; Mordret et al. 2017).

Although very robust to detect small changes in a medium (Froment et al. 2010; Weaver et al. 2011; Colombi et al. 2014), CWI lacks spatial resolution due to the inherent nature of coda waves. Statistical approaches can lead to the probability of a local change in a medium knowing the perturbation in the coda of a seismogram (Pacheco & Snieder 2005; Obermann et al. 2013) but the sensitivity kernels derived in these studies are smooth, dependent on the modal distribution of the waves forming the coda and on the statistical scattering properties of the medium which hamper a precise localization of the changes and proper estimate of their real amplitude.

In this work and a companion paper (Brenguier et al. 2019) we propose to overcome these limitations by using a new complementary method for monitoring seismic velocity variations based on the ballistic waves of the noise cross-correlations, instead of their coda waves. The first paper (Brenguier et al. 2019) deals with body waves while this paper focuses on surface waves application. Using ballistic waves means that, contrarily to coda-waves, we have accurate models for their propagation and therefore we can project the observed temporal perturbations of seismic velocities to specific regions at depth (Voisin et al. 2016, 2017). However, the clear limitation of using direct, ballistic waves is their strong sensitivity to noise source temporal variations (Colombi et al. 2014) and the fact that they exhibit smaller time-shift than coda waves, for the same perturbation. We use advanced frequency–time analysis and a dense seismic network coupled with offset and azimuthal averaging to mitigate these issues, but one still needs to carefully assess the stability of noise sources for such type of analysis.

Surface waves are the most easily retrieved phases in ambient noise correlations (Shapiro & Campillo 2004) because seismic noise sources are most often located at the surface and mainly generate surface waves. However, certainly because of the aforementioned drawbacks, only few attempts have been made to use direct surface waves from noise correlations to monitor the subsurface (Durand et al. 2011; de Ridder et al. 2014; Mordret et al. 2014b; Toyokuni et al. 2018). In this paper we describe the basics of passive ballistic surface wave monitoring using dense arrays. We are able to measure temporal changes of apparent velocities from both fundamental mode and

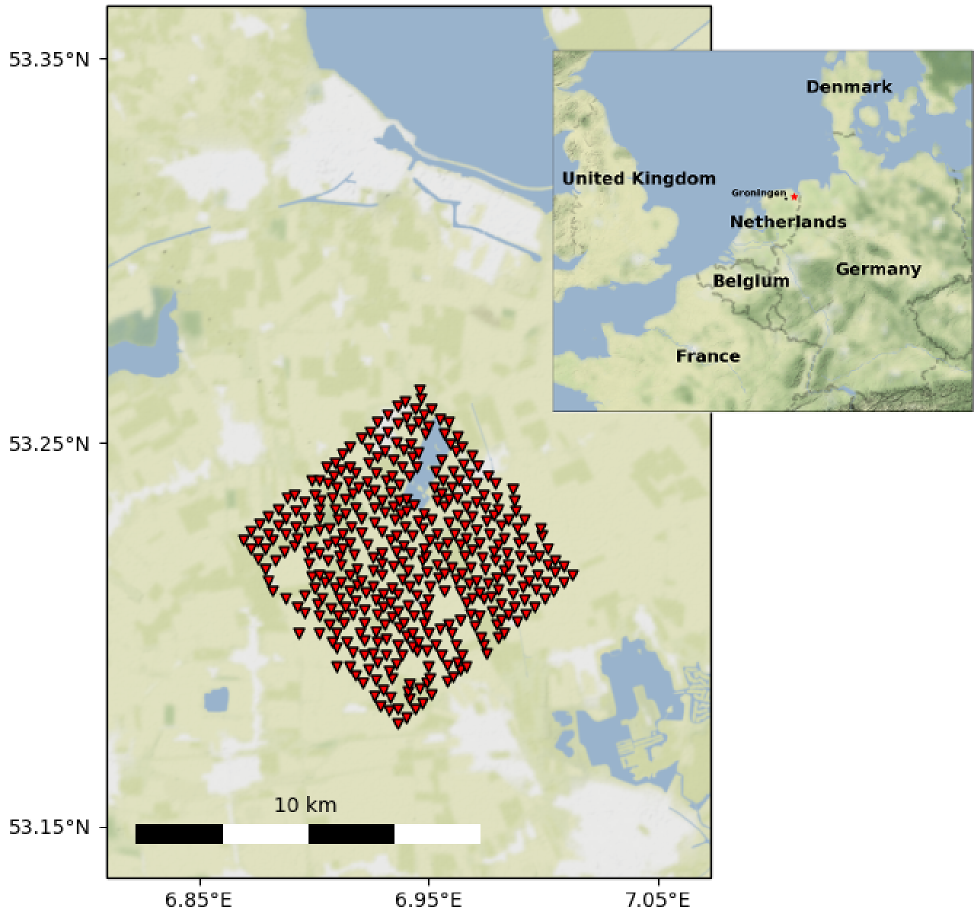


**Figure 1.** Map of the array of 417 sensors used in this study.

first overtone Rayleigh waves, which allows us to discriminate between changes localized in the shallower part or the deeper part of the subsurface, in good agreement with the P-wave monitoring results (Brenguier et al. 2019).

## 2 DATA

We use a network of 417 nodal short period seismic stations (3-component, 5 Hz Geospace) deployed in the Groningen area of the Netherlands, above the Groningen gas field (Fig. 1). The array was deployed for 30 days in 2017 from February 11 (day 42) to March 12 (day 71) and laid out as a regular square grid with an aperture of about 8 km and a nominal inter-station distance of 400 m. The original purpose of the array was to perform high-resolution ambient seismic noise tomography to characterize the near surface for seismic hazard assessment and ground motion

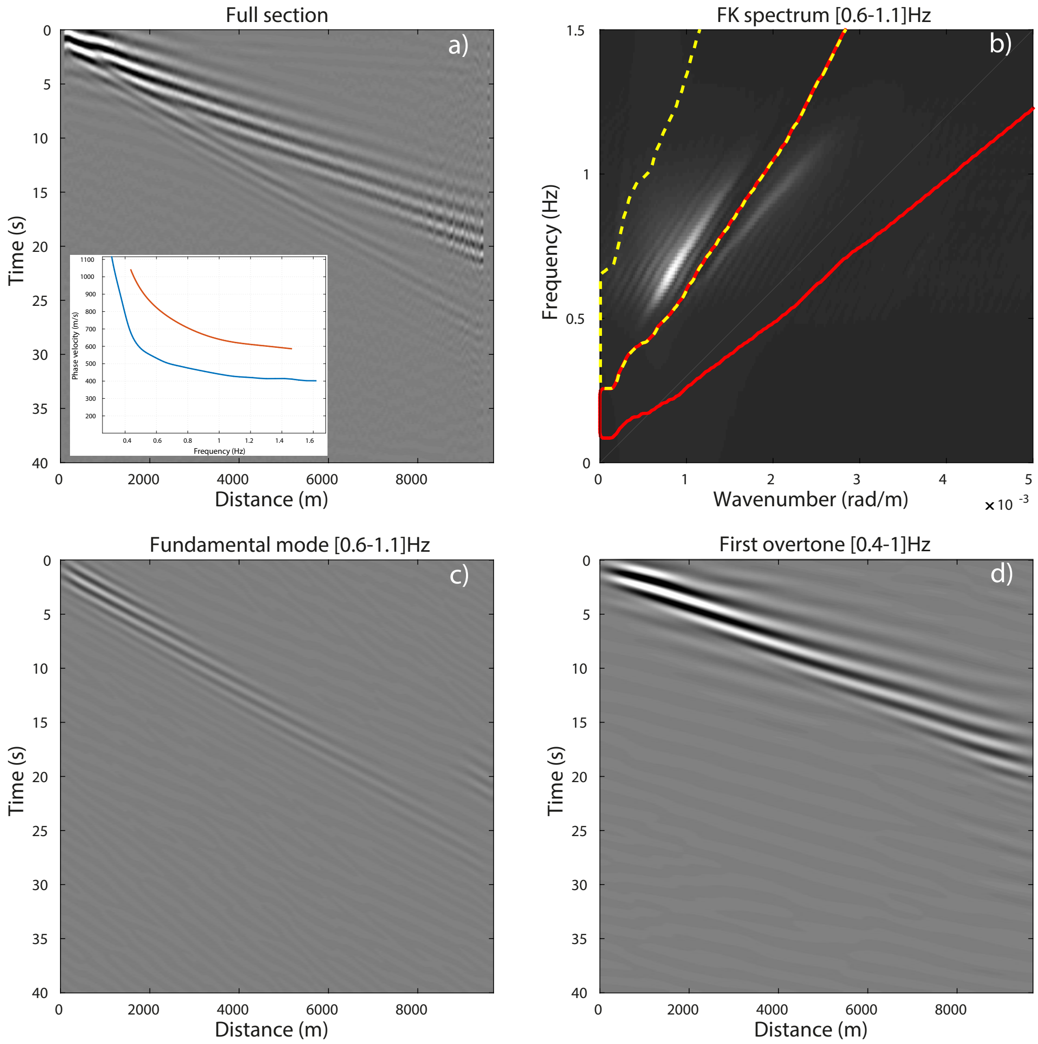


**Figure 2.** a) Full seismic section filtered between [0.6–1.1] Hz. The inset shows the phase velocity dispersion curves of the fundamental mode (blue) and the first overtone (red). b) FK diagram of the seismic section. The FK filter windows to extract the fundamental mode and the first overtone are shown in red and yellow, respectively. c) The FK-filtered fundamental mode band-pass filtered between [0.6–1.1]Hz. d) The FK-filtered first overtone band-pass filtered between [0.4–1.0]Hz.

prediction (Chmiel et al. 2019). The gas reservoir is located at about 3 km depth in the Permian sandstones of the Rotliegend Group, it is 250 m thick and covers a 2000 km$^2$ area. It is sealed by a Zechstein salt layer up to 1 km thick. Above the salt layer lays a $\sim$1 km thick Cretaceous Chalk formation capped with a 800 m thick Tertiary and Quaternary sediment cover, up to the surface (van Thienen-Visser & Breunese 2015). Bourne et al. (2018) show that the gas production in this field led to a 15 MPa average reservoir pore-pressure depletion since 1995 which is associated with seismicity rates exponentially increasing with time.

We follow Chmiel et al. (2019)'s procedure for the correlation computation. We average the causal and acausal sides of the correlations, then the symmetrized correlations are further stacked in 50 m inter-station distance bins, thanks to a continuous distribution of inter-station distances between 400 m and 8 km, to enhance the signal to noise ratio, to mitigate the azimuthal variations of noise sources and to help to converge closer to the true Green's function (Boué et al. 2013; Mordret et al. 2014a; Nakata et al. 2015). This procedure effectively approximates the propagating medium as a 1-dimensional medium. During the deployment, the main noise source in the considered frequency band comes from the direction of the North Sea, but significant energy arrival covers about 180 degrees, from South-West to North-East (Spica et al. 2018; Brenguier et al. 2019).

Finally, we construct one 30-days average seismic section which is used as the reference section and twenty-one 10-days moving average sections which are used as daily section for the monitoring. We use a causal stack where the section for day N is the stack of the data of day N with the 9 previous days. The resulting reference virtual seismic section, filtered between [0.6–1.1] Hz, is shown in Figure 2a). We can see the faster, higher amplitude and lower frequency first overtone travelling with a group velocity of about 450 m/s and the slower and less energetic fundamental mode travelling at a speed around 330 m/s. The FK spectrum of the section is shown in Figure 2b) and is used to pick the phase velocity dispersion curves of the two modes (Fig. 2a)). In the following, we perform the monitoring measurements on each mode separately. To do so, we apply two FK-filters to each of the 22 sections (the reference and the 21 daily ones) as described in Figure 2b-c-d). The FK-filtered sections are further windowed between travel-times corresponding to [250–380] m/s and [400–1000] m/s for the fundamental mode and the first overtone, respectively. We tested the effect of the FK-filters on the final velocity variation results: not using them slightly increases the uncertainties but does not change the overall results and interpretations.

## 3 METHODS

### 3.1 Phase-shift measurement with Cross-Wavelet transform

Measuring the travel-time shift induced by a localized seismic velocity perturbation on a dispersive surface-wave requires a frequency–time representation where one is able to estimate the instantaneous phase of a seismogram in the frequency–time domain (Corciulo et al. 2012). Continuous wavelet transform (CWT) has been extensively used in Earth Science for more than two decades to analyse the frequency–time behaviour of geophysical transient signals (e.g., Kumar & Foufoula-Georgiou 1994; Pyrak-Nolte & Nolte 1995; Labat 2005) and has originally been developed to analyse active seismic traces in seismic exploration (Morlet et al. 1982b,a). This section describes the use of wavelet-transform for ballistic surface wave monitoring. A similar approach can be used for CWI applications and is the subject of a subsequent paper (Mao et al. 2019b).

The CWT of a signal $s(t)$ is defined as the correlation or inner product of $s(t)$ with a particular set of functions $h_{a,b}(t)$ such as

$$\mathbf{WT}[s(t)](a,b) = \int_{-\infty}^{\infty} s(t) h^*_{a,b}(t) dt \,, \tag{1}$$

where

$$h_{a,b}(t) = \frac{h[(t-b)/a]}{\sqrt{|a|}} \,. \tag{2}$$

In these expressions, $a, b \in \mathbb{R}$, with $a \neq 0$. The $*$ symbol denotes the complex conjugate. The elements of the wavelet basis $h_{a,b}(t)$ are created by dilating and translating the mother wavelet $h(t)$ by the dilation parameters $a$ (called scale and equivalent for frequency) and the translation parameters $b$. The pre-factor $\sqrt{|a|}$ ensures norm-squared normalisation. Practically, we used the CWT function from the MATLAB2018a Wavelet Toolbox to build our algorithm.

In the following analysis, we use the complex analytic Morlet wavelet (Morlet et al. 1982b,a; Teolis & Benedetto 1998) composed of a harmonic function windowed by a Gaussian filter. In the Fourier domain the Morlet wavelet is defined as:

$$\Psi(a\omega) = \pi^{-1/4} e^{-(a\omega-\omega_0)^2/2} H(a\omega) \,, \tag{3}$$

where $H$ is the Heaviside step function, $a$ is the scale and $\omega_0$ the central frequency. Here, we use $\omega_0 = 6$ Hz as default value.

The resulting Morlet CWT is a 2D complex function which has both amplitude and phase information and has an optimum resolution both in time and frequency with the smallest possible

Heisenberg uncertainty. It can be shown that the maximum of the CWT amplitude along the scale direction defines the group velocity dispersion curves of the transformed time-series (Pyrak-Nolte & Nolte 1995).

To compare two dispersive time-series by estimating their common power and phase relation, we use the cross-wavelet transform (Grinsted et al. 2004) which can be seen as a frequency–time cross-correlation. Let $r(t)$ be a reference seismic trace and $c(t)$ the current seismic trace we want to compare with $r(t)$. The cross-wavelet transform of $r$ and $c$ is

$$\mathbf{XWT}[r(t), c(t)](a,b) = \mathbf{WT}[r(t)](a,b)\mathbf{WT}^*[c(t)](a,b) = |A|e^{i\Delta\phi}\,, \tag{4}$$

where $|A|$ is the amplitude power of the cross-wavelet transform and its phase is given by the phase difference between $\mathbf{WT}[c(t)]$ and $\mathbf{WT}[r(t)]$ such as $\Delta\phi = arg\left(\mathbf{WT}[r(t)]\right) - arg\left(\mathbf{WT}[c(t)]\right)$.

The amplitude power of the cross-wavelet transform shows where both time-series have common high amplitudes (Fig. 3d). Another useful measure of the resemblance between the two waveform in the frequency–time domain can be defined by the wavelet coherence (Fig. 3b):

$$\mathbf{WCoh}[r(t), c(t)](a,b) = \frac{|\mathcal{S}\left\{a^{-1}|\mathbf{XWT}[r(t), c(t)](a,b)|^2\right\}|^2}{\mathcal{S}\left\{a^{-1}|\mathbf{WT}[r(t)](a,b)|^2\right\}\mathcal{S}\left\{a^{-1}|\mathbf{WT}[c(t)](a,b)|^2\right\}}\,, \tag{5}$$

where $\mathcal{S}\left\{\cdot\right\}$ is a 2D smoothing operator over the scales $a$ and delays $b$. Here, we used a Gaussian smoothing window in the delays direction and a moving average (boxcar window) in the scales direction. The smoothing is necessary to avoid having a coherence of one for every samples. In traditional time-windowed Fourier transform methods, the smoothing is handled by defining an additional time-window length. The wavelet coherence can be seen as a local correlation coefficient in the frequency–time domain and is bounded between [0 1]. Finally, the time-shift $\Delta t$ in the frequency–time domain (Fig. 3c) between the two waveforms can be computed by

$$\Delta t(a,b) \equiv \Delta t(f,U) = \frac{\Delta\phi}{2\pi f}\,, \tag{6}$$

where $f$ is the frequency and $U$ the group velocity obtained by $U = D/t$, with $D$ the distance between the source and the receiver. However, the time-shift can only be reliably estimated where

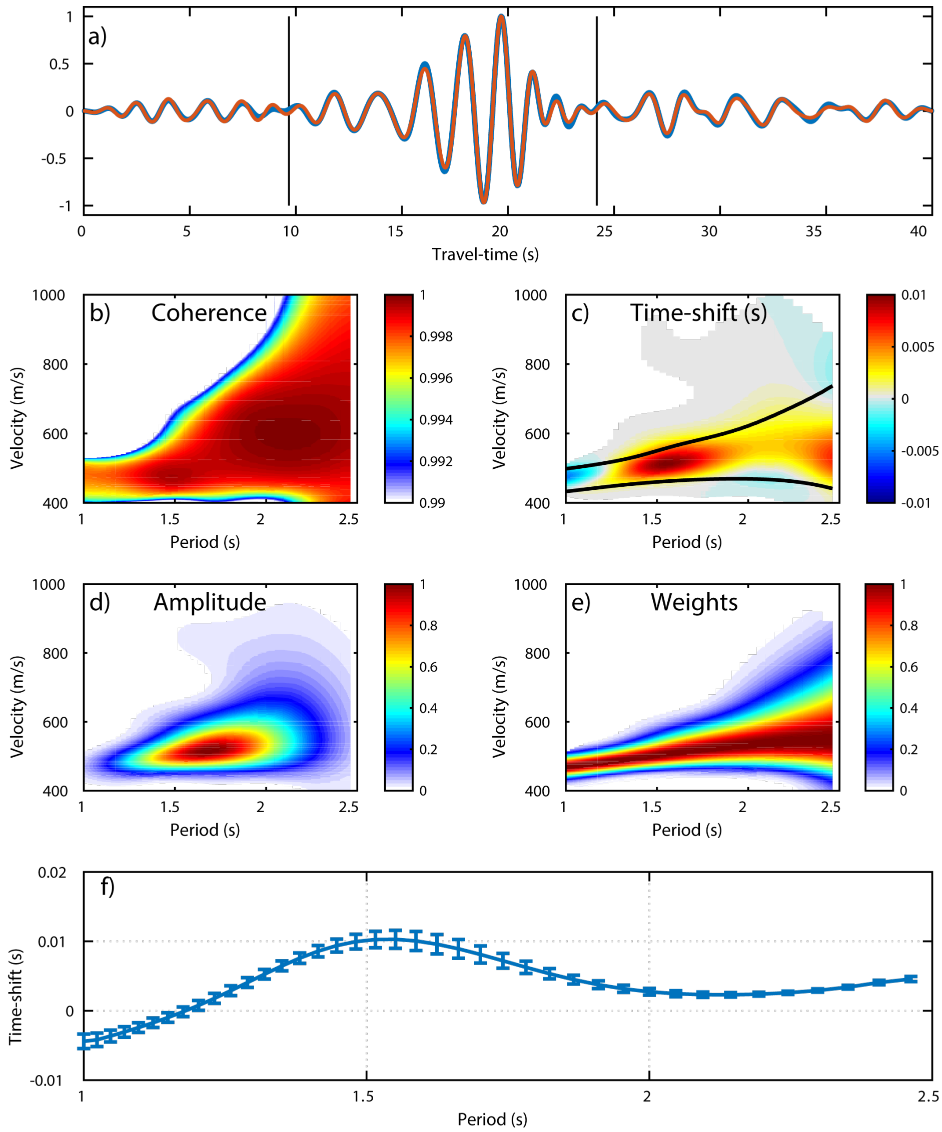


**Figure 3.** a) Reference (blue) and current (orange) binned correlations at 9 km distance, FK-filtered around the first overtone. The vertical black lines show the analysis window. b) Wavelet Coherence between the traces in a). c) The time-shift between the two traces multiplied by the weight function shown in e). The black contour shows where the weights are larger than 0.1. d) The normalised amplitude power of the cross-wavelet transform: $|A|$. e) The weight function. f) The weighted-average frequency-dependent time-shift, the errorbars show one standard deviation of the average.

the amplitudes of both reference and current traces are largely above the noise level, i.e., where $|A|$ is large enough. Following Fichtner et al. (2008), we design a coherence weighting scheme (Fig. 3e) that allows us to accurately extract the time-shift between the two waveforms as a function of the frequency:

$$\mathcal{W}(f,U) = (log(1+|A|)/\max_f log(1+|A|))^2 \qquad \text{if } WCoh > 0.95 \ \& \ |A|/\max_{f,U}|A| > 0.01, \quad (7)$$

$$\mathcal{W}(f,U) = 0 \qquad \text{otherwise.} \quad (8)$$

We finally obtain the frequency-dependant time-shift $\delta t(f)$ between the two waveforms by computing the weighted average of $\Delta t(f,U)$ by $\mathcal{W}(f,U)$ along the group velocity axis. We repeat this operation for every distance bins, every days and for both FK-filtered fundamental and first overtone.

### 3.2 Relative phase velocity change estimation

From the time-shifts measured at each frequency and each distance along the virtual seismic section, we can estimate the frequency-dependant relative phase velocity change $\delta C_i^m/C_0^m$ for each day $i = 1..21$ ($i = 0$ stands for the average over the 30 days) and each considered phase $m = 0, 1$ (for the fundamental mode and the first overtone, respectively) following the approach of Brenguier et al. (2019). In this companion paper, Brenguier et al. (2019) showed that the relative velocity change can be computed as the (weighted) linear regression of the time-shifts $\delta t$ along the offset $x$ (Fig. 4) multiplied by the velocity of the considered phase:

$$\frac{\delta C_i^m}{C_0^m}(f) = -C_0^m(f)\frac{\Delta \delta t_i^m(f,x)}{\Delta x}\Bigg|_{x=x_{min}}^{x=x_{max}}, \quad (9)$$

where $\Delta Y/\Delta x$ stands for the linear regression of $Y$ along $x$ and $x_{min}$ and $x_{max}$ are the offset bounds between which the regression is performed. We will develop more in the Results section on how to chose these bounds. The standard errors of the linear regression gives the uncertainty of the relative velocity change.

### 3.3 Depth-dependent relative shear-wave velocity change

Lesage et al. (2014) were the first to attempt a depth inversion of differential dispersion curves for relative shear-wave velocity changes. We use a similar approach here to resolve the velocity change at depth at our studied area. As shown by Haney & Tsai (2017) using a thin-layer finite-element

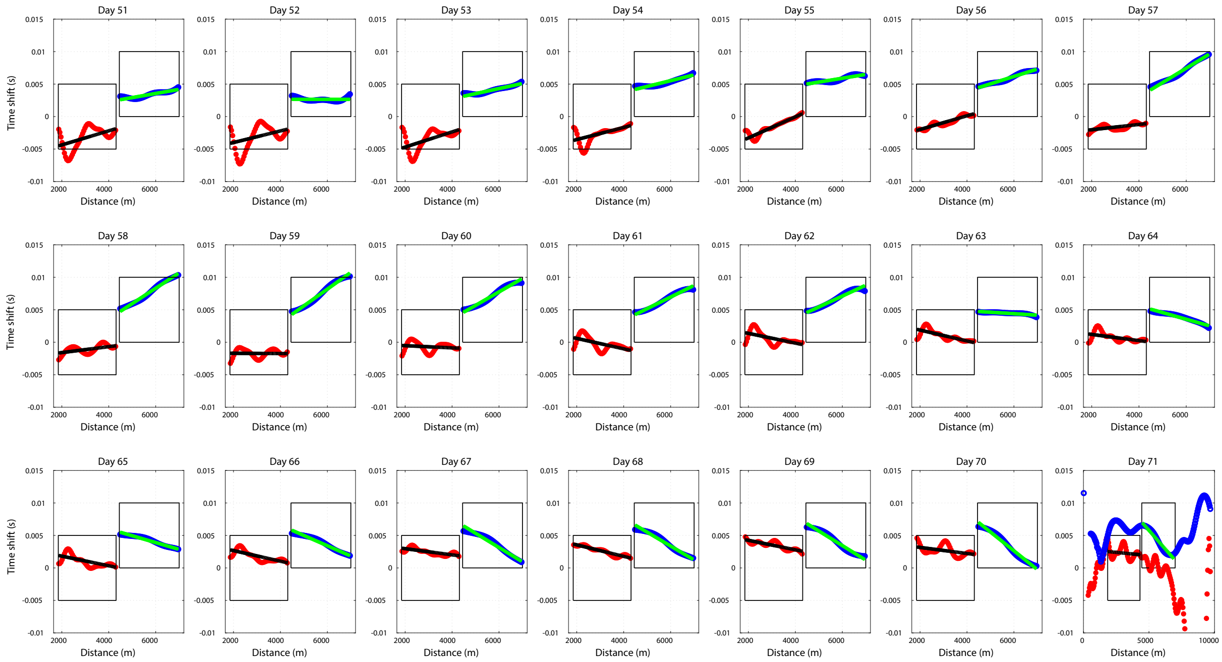


**Figure 4.** Daily time-shifts $\delta t^m(x)$ averaged over the frequencies for the fundamental mode (red dots) and the first overtone (blue dots) and the linear regressions used to estimate the relative phase velocity variations in black and green for the fundamental mode and the first overtone, respectively. The black boxes show the distance ranges over which the regression is performed. The results for the first overtone have been shifted vertically by 0.005 s to avoid clutter. For the day 71, we show the measurements along the whole offsets range.

method approach, the relative change in Rayleigh wave phase velocity $\mathbf{C}(f)$ for any given mode, at different frequencies (Fig. 5), due to a relative change in shear-wave velocity $\boldsymbol{\beta}(z)$ at depth is given by:

$$\frac{\delta \mathbf{C}}{\mathbf{C}}(f) = \mathbf{K}(f,z)\frac{\delta \boldsymbol{\beta}}{\boldsymbol{\beta}}(z)\,, \tag{10}$$

where $\mathbf{K}$ is a depth sensitivity kernel, $f$ the frequency and $z$ the depth. Equation 10 holds if one assumes that either (1) Poissons ratio and density are fixed or (2) P-wave velocity and density are fixed. In each case, the sensitivity kernel has to be adapted (see Haney & Tsai 2017, for details) and we modified Haney & Tsai (2017)'s code to output the corresponding $\mathbf{K}$ computed from an average velocity model of the area (Chmiel et al. 2019). This average model is in good agreement with local borehole measurements (Kruiver et al. 2017) and predicts properly the average phase velocity dispersion curves for both the fundamental mode and the first overtone. In this work, we chose to fix the P-wave velocity and the density.

The relative shear-wave velocity perturbation can therefore be retrieved using a simple weighted-damped least squares inversion (Haney & Tsai 2017). Following Haney & Tsai (2017), we define the data covariance matrix as a diagonal matrix with the relative phase velocity uncertainties on the diagonal ($\mathbf{C_d} = \boldsymbol{\sigma}_d \mathbf{I}$) and the model covariance matrix as:

$$\mathbf{C_m}(i,j) = \sigma_m^2 \exp\left(-|z_i - z_j|/\lambda\right), \tag{11}$$

where $\sigma_m = \gamma \bar{\sigma_d}$ is the model standard deviation ($\gamma$ is a user-defined tuning factor and $\bar{\sigma_d}$ is the average of the data uncertainties), $z_i$ and $z_j$ are the depths at the top of the i$^{th}$ and j$^{th}$ layers, and $\lambda$ is a correlation length along depth. The parameters $\gamma$ and $\lambda$ are defined through a systematic grid-search of the data residual evolution with respect to $\gamma$ and $\lambda$ trial values, using a L-curve criterion (Hansen & OLeary 1993). The depth distribution of the shear-wave perturbations is obtained by solving the following system

$$\begin{bmatrix} \mathbf{C_d^{-1} K} \\ \mathbf{C_m^{-1}} \end{bmatrix} \frac{\delta \boldsymbol{\beta}}{\boldsymbol{\beta}} = \begin{bmatrix} \mathbf{C_d^{-1}} \\ \mathbf{0} \end{bmatrix} \frac{\delta \mathbf{C}}{\mathbf{C}}.$$

## 4 RESULTS

The fundamental mode is analysed in the [0.6 - 1.1] Hz frequency band and the first overtone in the [0.4 - 1.0] Hz frequency band, where most of their energy is concentrated (Fig. 2b). The fundamental mode exhibit large amplitudes at frequencies lower than 0.5 Hz (Chmiel et al. 2019) but at these frequencies, the wavelengths become large compared to the size of the array which impedes the measurement of the time shift and reduces the distance range on which the linear regression can be performed. As shown in Figure 4, the time-shifts data do not exhibit a linear trend for the whole range of distances. At long distances, the $\delta t_i^m(x)$ measurements strongly oscillate (starting around 6.5-7 km) because of the lower signal to noise ratio of the stacked correlations which are much less numerous for these ranges. At short distance, we also observe rapid oscillations of the

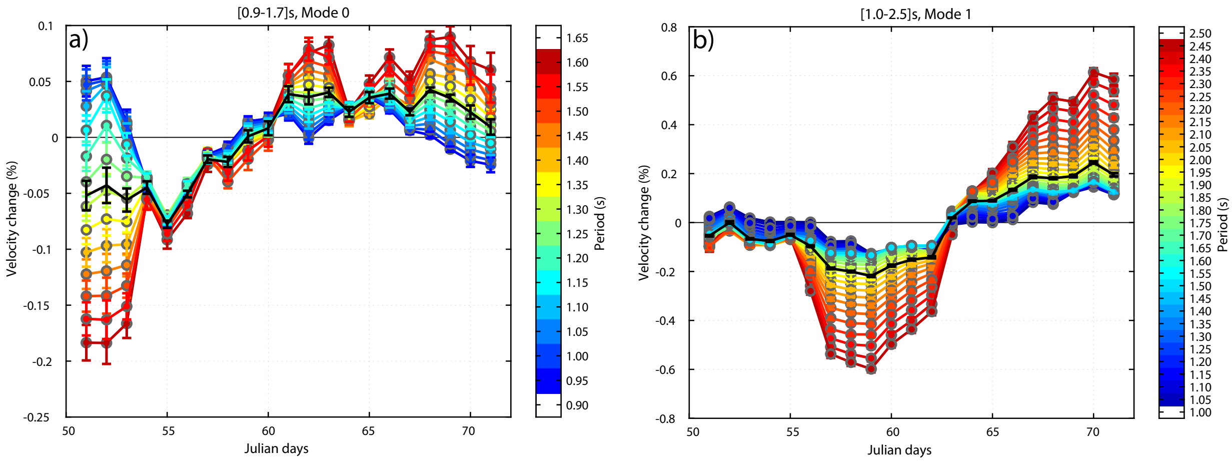


**Figure 5.** left) Daily, period-dependant relative phase velocity changes for the fundamental mode. right) Daily, period-dependant relative phase velocity changes for the first overtone. Note the difference in amplitude between the two modes. The black curves are obtained by averaging the time-shifts $\delta t_i^m(f, x)$ over the frequencies before performing the linear regression (shown in Fig.4).

time-shifts for both fundamental mode and overtone. However, the fundamental mode measurements (red dots in Fig. 4) seems to stabilize at shorter distance ($\sim$2 km) than the overtone ($\sim$4.5 km). We hypothesize that this effect is a consequence of performing the time-shift measurements on waves in the near field where wave interference may occur. The dominant frequencies of 0.8 Hz and 0.6 Hz give wavelengths on the order of $\sim$600 m and $\sim$1400 m for the fundamental mode and the first overtone, respectively. The measurements are therefore stabilizing around three wavelengths for both phases, a distance at which the near-field effects become negligible. We chose to perform the linear regressions along the distances corresponding to three to seven wavelengths. In the case of the overtone, seven wavelengths correspond to a distance larger than 7 km, we therefore restrict the maximum distance for this phase at 7 km. Extending the linear regression for the fundamental mode to 7 km would slightly change the estimated values of $\delta C_i^0/C^0$ but has little effect on the final estimation of the depth and amplitude of the shear-velocity changes.

Figure 5 shows the temporal variations of phase velocity for the two modes at different frequencies. Except for the three first days, the fundamental mode exhibit variations smaller than $\pm 0.1\%$ at all frequencies. In general, lower frequencies show larger velocity changes which suggests that the changes are happening deeper in the subsurface rather than shallower. This is confirmed by the shape of the depth sensitivity kernels for the fundamental mode (Fig. 6). In contrast, the overtone

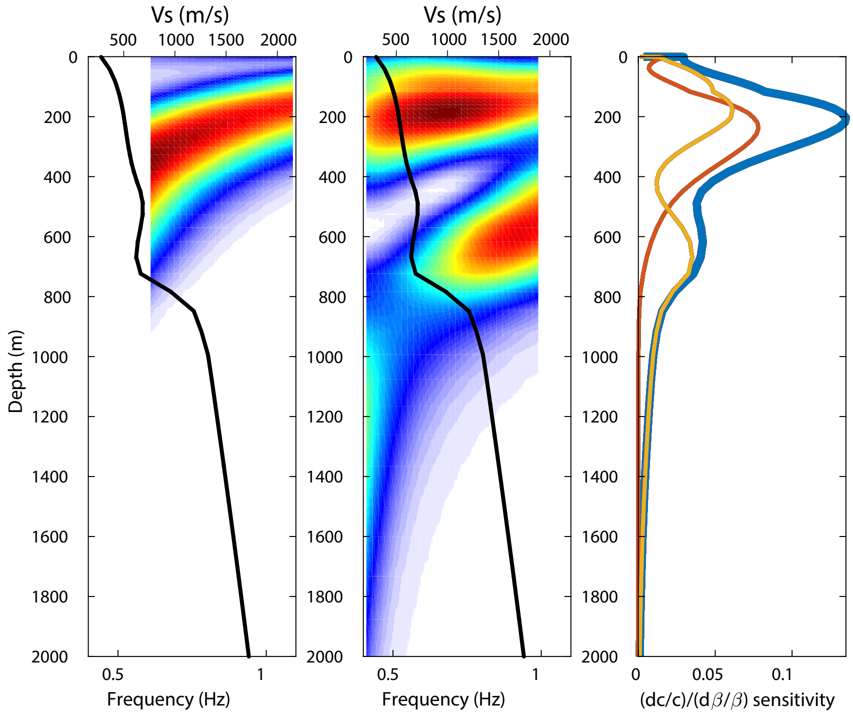


**Figure 6.** Depth sensitivity kernels for relative perturbations in shear-wave velocity with respect to relative perturbations in phase velocity for the fundamental mode (left) and the first overtone (middle). The right panel shows the frequency-averaged kernels (fundamental mode in red, first overtone in yellow) and their sum (in blue) showing the total extent of depth sensitivity when combing the two modes. The (normalized) shear-wave velocity model used for the computation is shown by the black curves.

exhibits much larger temporal variations with amplitudes up to 0.6% at low frequency. For these frequencies lower than 0.5 Hz (above 2 s of period), the sensitivity of the overtone displays two maxima: a large amplitude one around 200 m depth and a lower amplitude one below 1000 m depth. The shallow sensitivity region overlaps with the sensitivity of the fundamental mode. The fact that the fundamental mode shows only small variations suggests that the large variations detected by the first overtone at low frequency are located deep in the subsurface.

These observations are confirmed by the joint inversion of the differential phase dispersion curves (Fig. 7). We used $\gamma = 100$ and $\lambda = 250m$ as smoothing and damping parameters. The median misfit reduction for the whole time period is 81%. The fit to the data is good for every day meaning that we manage to find a model of relative shear-wave velocity change at depth that is consistent with both fundamental mode and first overtone daily observations. From Figure 7, we can see that the overtone data at low frequency explain most of the variance of the model. The final

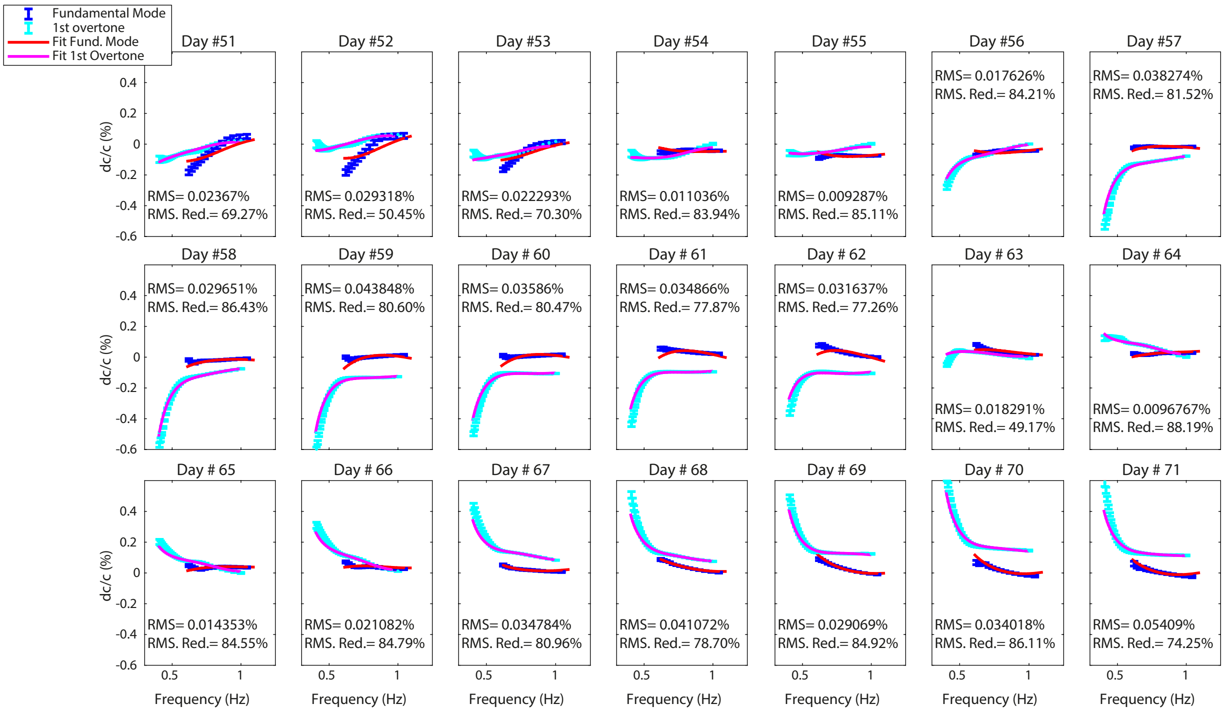


**Figure 7.** Daily differential phase velocity dispersion curves for the fundamental mode and the first overtone with their uncertainties (blue and cyan curves, respectively). The fit to the data after inversion is shown by the inverted dispersion curves in red and magenta for the fundamental mode and the first overtone, respectively. The daily misfit value as well as the misfit reduction from $\delta C/C = 0$ are shown in each panel.

time-lapse results (Fig. 8) indeed show that the largest shear-wave variations (reaching $\pm$ 1.5%) are located below 800 m in the faster layer of the Chalk Group formation, while smaller variations are observed in the shallower North Sea Group sediments (Fig. 9 Kruiver et al. 2017; Chmiel et al. 2019). The decrease of the amplitude below 1600 m is mostly due to the disappearance of the sensitivity of the first overtone at these depths and we cannot rule out large velocity changes deeper in the subsurface.

Velocity variations in the near-surface are shown in Figure 9 with a different color scale to highlight the finer details. The shallow time-lapse results show variations on the order of $\pm$ 0.2% in the near surface ($\sim$50 m depth) with a large decrease of velocity between day 51 and day 55 followed by a slow recovery until the end of the studied period. The velocity decrease propagates deeper and deeper at depth along the 20 days of record with an apparent vertical velocity of about 10 m/d.

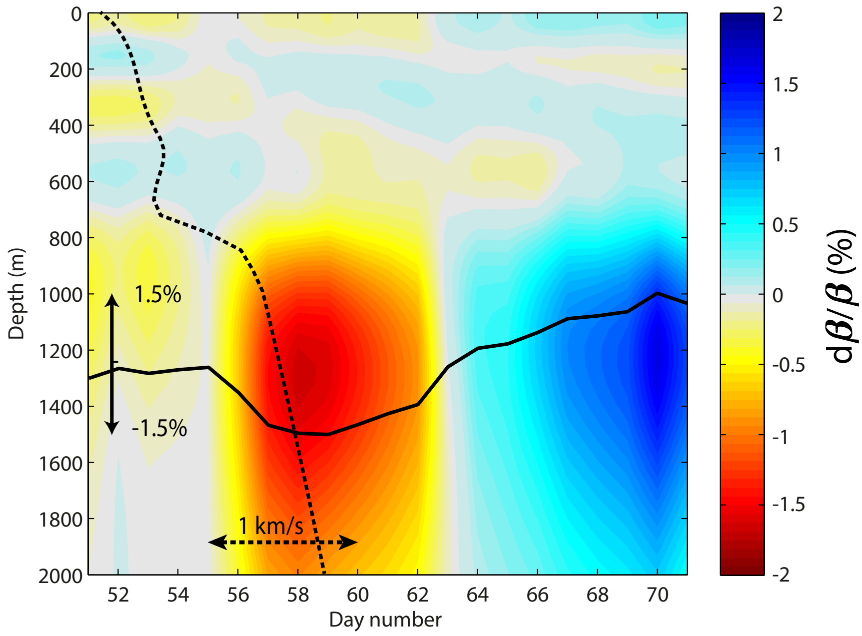


**Figure 8.** Depth-dependent relative shear-wave changes obtained by jointly inverting the frequency-dependent relative phase velocity variations of the fundamental mode and the first overtone. The average velocity change between 1000 m and 1500 m is shown by the plain black curve. Most of the changes happen in the Chalk layer below 1000 m depth. The average Vs model of the area is shown in dotted black curve for reference with the scale denoted by the dotted arrows.

## 5 DISCUSSION AND CONCLUSION

Ballistic wave travel-time from noise correlations are strongly sensitive to the noise sources distribution and its azimuthal variations during the monitoring period. For the same dataset, Brenguier et al. (2019) checked that the azimuthal variations of the noise could not induce travel-time uncertainties larger than 0.5%. Moreover, the stacking procedure that we used is partly an azimuthal stacking and therefore helps to reduce the noise sources influence on the phase-shift measurements. The large velocity change that we observe below 1000 m cannot be explained by noise sources biases alone. The amplitudes of the shallow variations are less strong and therefore could be contaminated by potential sources effects. However, the depth migration of the velocity reduction cannot be caused by noise sources variability.

Noise sources static spatial distribution inhomogeneity also biases the amplitudes and phases of both fundamental mode and first overtone; with a stronger effect on the first overtone (Kimman & Trampert 2010). While this static effect has no influence on the monitoring measurements,

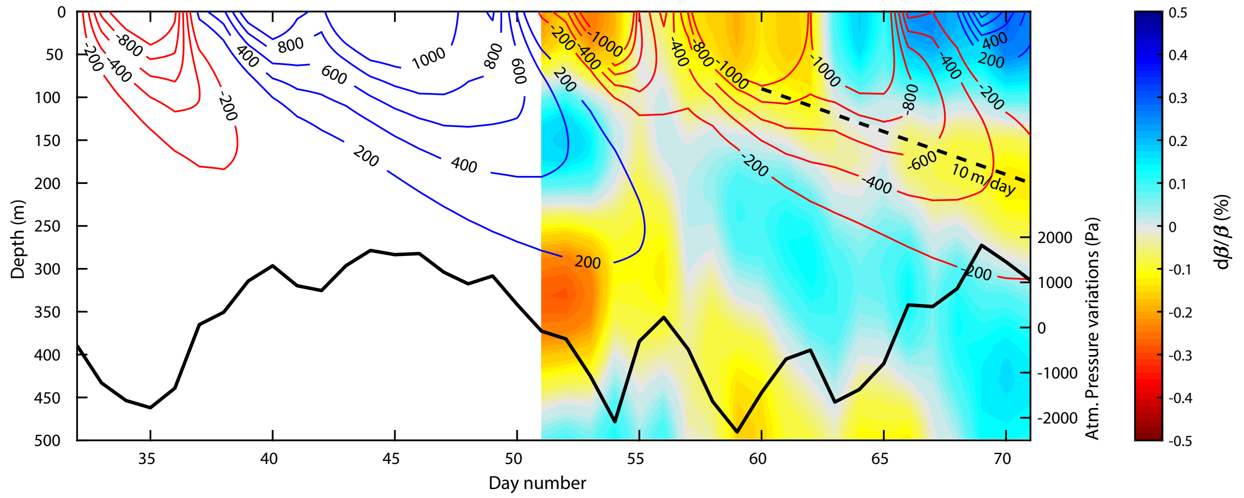


**Figure 9.** Near-surface depth-dependent relative shear-wave changes obtained by jointly inverting the frequency-dependent relative phase velocity variations of the fundamental mode and the first overtone. The velocity of 10 m/d, fitting the move-out of the velocity decrease is shown by the dotted line. The atmospheric pressure near the studied site is shown by the thick black line for the period of the study. The red contours correspond to effective pressure decrease, the blue contours correspond to effective-pressure increase.

because we are interested in relative changes, it may still induces an error on the inverted results. The depth sensitivity kernels that we are using for the inversion (Fig. 6) assume true fundamental and first overtone Rayleigh wave. Kimman & Trampert (2010) showed that the relative errors on the first overtone can be up to few percent (less for the fundamental mode), meaning that the kernels we use are off by a similar amount. This results in uncertainties on the depth location and amplitude of the changes in the shallow part on the order of few meters and about 0.02%, respectively.

To asses the sensitivity and the contribution of each dataset on the final result we perform a set of tests by inverting separately the fundamental mode and the first overtone dispersion curves (Fig. 10). In addition to these tests, we perform a second set of inversions by forcing the velocity variations to be located only in the first 500 m of the subsurface. To do so, we add to the model covariance matrix a damping of the velocity variations increasing exponentially with depth. The parameter of the exponential decay is chosen so that the velocity changes vanish bellow 500 m depth. For each of the eight tests, the misfit reduction, indicating the quality of the fit to the data and the amount of data explained by the model is shown in each panel of Figure 10. The individual daily fits to the data are shown in Supplementary Material Figures S1 to S8. A first observation is that the results obtained in Figure 9 and in Figure 8 in a lesser extent can only be found by inverting jointly the fundamental mode and the first overtone data. Secondly, although the first overtone has shallow sensitivity at low frequency (Fig. 6), changes bellow 800 m depth are required to properly fit the low frequency data. Changes alone above 500 m cannot fit the low frequency part of the overtone dispersion curve. The high frequencies (above 0.6 Hz) of the overtone mostly constrain changes in the first 800 m of the subsurface. If only the low frequency part of the overtone data is taken into account, the deep velocity changes are smeared between 300 m and 2 km depth. It is only the combination of the full bandwidth of the fundamental mode and the first overtone that localizes the large velocity changes in the Chalk layer, below 800 m depth.

Observing large velocity variations in the Chalk layer and smaller variations in the Tertiary and Quaternary sediments is in good agreement with the observations made with ballistic P-wave on the same dataset (Brenguier et al. 2019). On one hand, the P-wave refracted at the top of the Chalk layer exhibits small variations during the first four days then its speed increases by $\sim$1% on days 55-56 before stagnating or slightly decreasing during the rest of the analysed period. On the other hand, the direct P-wave, which is sampling the first 200 m of the subsurface, shows a small decrease of velocity of about -0.25% during the first 12 days, then a 0.1% recovery. The same pattern is observed with S-wave in the near-surface. It has to be noted that the reference used in the P-wave study and the current work are different. Therefore, only the variations of velocity changes and their relative amplitudes can be compared. In the Chalk layer, the anti-correlation between the S-wave and the P-wave velocity change, with similar amplitudes, could suggest a saturation effect (Fores et al. 2018). However, in the Netherlands it is most probable that the ground is fully saturated at these depths, ruling out this interpretation. Changes originating from deeper in the subsurface might be possible, but we do not have any other independent information from the exploitation of the gas field to confirm or infirm the deep nature of the observed changes in the Chalk layer. Tidal-induced strain variations can induce seismic velocity changes. However, such changes have been shown to be small and have mainly diurnal and semi-diurnal effects (Reasen-

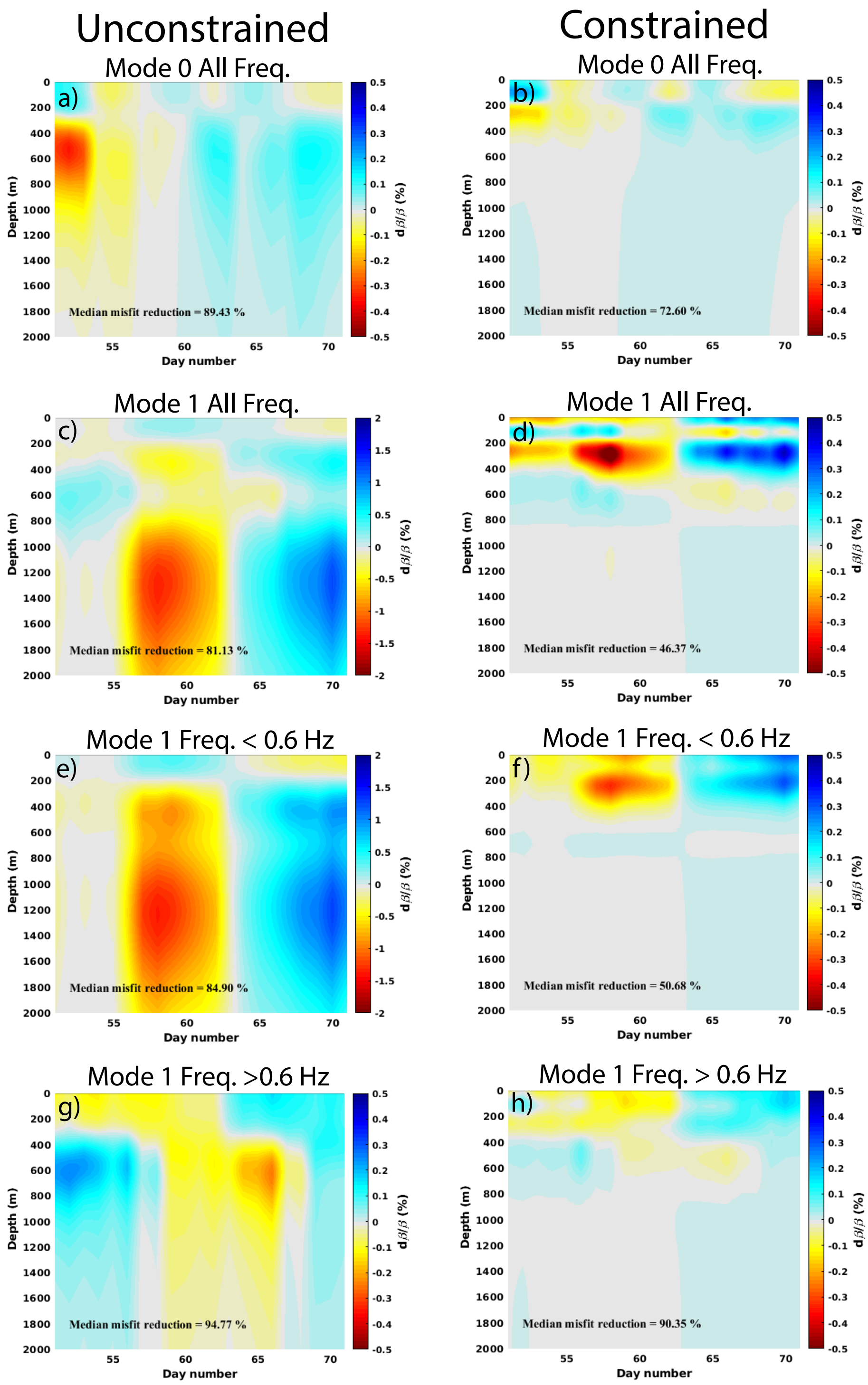


**Figure 10.** Sensitivity tests. Inversion of a single mode, with and without constrain, for different frequency bands. The median misfit reduction over the 20 days of the study is shown at the bottom of the panels. A misfit reduction below 70% indicates a poor fit to the data. Note the different color scale for panels c) and e). The corresponding individual daily fits are shown in Fig. S1 to S8 of the Supplementary Material.

berg & Aki 1974; Yamamura et al. 2003; Mao et al. 2019a). Our observations do not exhibit such a periodicity, neither in the deep part of our model nor in the near-surface. Longer periods (around 15 days) exist in the oceanic loading signal but we would expect the loading-induced strain to affect the whole column of sediment and more particularly the less consolidated ones in the near-surface, which is not what we observe. Another hypothesis is that the low frequency measurements for the first overtone are biased by near-field effects which would produce an over-estimation of the amplitude of velocity variations. However, the fact that the refracted P-wave (measured in the far field) senses large changes indicates that the observed deep variations may be real.

One of the main factor that can influence the seismic velocities in a poroelastic medium is variations of effective pressure. These variations can come from two sources in a environment such as the one studied here: normal stress variations and pore pressure variations. The normal stress variations can be induced by atmospheric pressure variations, while the pore pressure variations can be induced by rainfalls. Large variations of shear velocity of few percent have already been observed after strong rain events (e.g., Sens-Schönfelder & Wegler 2006; Miao et al. 2018; Viens et al. 2018; James et al. 2019) even though the amount of decrease depends on the initial state of the soil. During the monitoring period a rainfall event happened during days 51 to 54 with 40 mm of water (16 mm alone on day 54) following a 2 weeks period without rain. This strong rain event induces an increase in pore pressure in the subsurface on the order of 10-100 Pa which diffuses at depth with time. Atmospheric loading variations varying around $\pm$ 2 kPa (Fig. 9) are accompanying the rain falls (KNMI 2019). We use the model of Roeloffs (1988), extended by Talwani et al. (2007) to model the diffusion of effective pressure variations at depth, given loading variations at the surface from the rain and the atmospheric pressure. The excess pressure $P(t, r)$ at time $t$ and depth $r$ is given by:

$$P_i(t, r) = \sum_i^n \delta p_i \operatorname{erfc}\left[\frac{r}{\sqrt{4c(n-i)\delta t}}\right], \tag{12}$$

where $\delta p_i$ is the relative load variation for the day $i$, $c$ is the hydraulic diffusivity, $n$ the number of days from the beginning of the record and up to time $t$, $\delta t$ the time increment and $\operatorname{erfc}$ is the complementary error function. The hydraulic diffusivity is a free parameter and we chose

$c = 0.02m^2/s$ in order to fit the move-out of the shear-wave velocity decrease (Fig. 9). The values obtained for the hydraulic diffusivity ($2 \cdot 10^{-2}m^2/s$) and conductivity ($10m/d$) are consistent with the geology of the quaternary deposits in the subsurface (TNO 2019). Moreover, a variation in effective pressure is consistent with the discrepancy in velocity variations amplitude between Vp and Vs, Vp being less sensitive to effective pressure changes than Vs in unconsolidated sediments (e.g. Zimmer et al. 2002).

The maximum change in pore-pressure is about 1 kPa near the surface and decays at depth and in time to about 0.4 kPa at the end of the monitoring period at about 200 m depth. (Fig. 9). Kruiver et al. (2017) propose a relationship between the shear velocity ($\beta$) and the confining stress ($\sigma_0$) of the form

$$\beta = \beta_0 \left(\frac{\sigma_0}{P_0}\right)^{\gamma}, \tag{13}$$

where $\beta_0$ is the shear-wave velocity at the surface, $P_0$ is the atmospheric pressure and $\gamma$ is an exponent depending on the geology. Given the local variability in the parameters $180m/s < \beta_0 < 270m/s$ and $0.1 < \gamma < 0.43$ (Kruiver et al. 2017), we can estimate the sensitivity of $\beta$ to changes in effective pressure $P_e$, $8 \cdot 10^{-5} < d\beta/dP_e < 5 \cdot 10^{-4}$ and the range of expected $d\beta/\beta$ with

$$\frac{d\beta}{\beta} = \frac{d\beta}{dP_e}\frac{dP_e}{\beta}. \tag{14}$$

Taking $\beta = 350$ m/s at 50 m depth, an effective pressure of 300 kPa (assuming a soil density of 1600 kg/m$^3$) and a variation of effective pressure of 1 kPa, we obtain values of $d\beta/\beta$ ranging from $0.02\%$ to $0.15\%$. This indicate that our results are in good agreement with the upper ranges of $\beta_0$ and $\gamma$.

One of the main limitation of this new passive monitoring approach is the need for dense seismic arrays with a relatively large aperture to be able to perform a robust linear regression of the time-shifts along the offsets. Although such dense arrays are more and more common (e.g., Mordret et al. 2014b; Nakata et al. 2015; Ben-Zion et al. 2015), one would ideally like to perform the monitoring measurements on signals from a single pair of stations. One could therefore take advantage of sparse, but permanent or long-term seismic networks, the same way they are used for CWI. This will lead to purely passive 4D seismic tomography studies, which will be the logical next step from the present analysis. It can be done because we can always measure the time-shift between 2 non-synchronous correlations from the same station pair using Equation 6. The methodology to measure this time-shift is described in detail by (Mao et al. 2019b). The relative (phase) velocity variation can then be estimated with

$$\frac{\delta v}{v_0} = -v_0 \frac{\delta t}{D} \,. \tag{15}$$

Here, $v_0$ is the phase velocity of the considered (ballistic) wave and $D$ corresponds to the inter-station distance. However, without the averaging scheme presented in this paper, the ballistic waves can be strongly sensitive to variations in the seismic noise sources positions and properties which can mask the changes of interest in the subsurface.

We present in this study a novel approach to monitor the seismic velocity temporal changes using ambient noise correlations. Instead of measuring delays in the coda part of single pair of stations seismograms, we evaluate the time-shift of the ballistic Rayleigh waves, retrieved from a dense seismic network, as a function of the propagation distance, to get the relative velocity changes. Using a wavelet-transform processing, we are able to extract frequency-dependent time-shifts for different modes. This enables us to invert the corresponding differential dispersion curves into 1D depth-dependent relative shear-wave velocity variation profiles. The information from two different Rayleigh wave modes helps to constrain the location of the changes at depth. The observed shallow temporal velocity changes, reaching $\pm 0.2\%$, are caused by a decrease of effective pressure diffusing in the ground following heavy rainfalls. This method, generalized to any ballistic waves (Brenguier et al. 2019), paves the way to high temporal and spatial resolution monitoring studies and make passive time-lapse tomography of dynamic geological targets, such as volcano magma chambers, active tectonic faults or industrially exploited reservoirs, possible.

**ACKNOWLEDGMENTS**

AM acknowledges support from the National Science Foundation grant PLR-1643761. ISTerre is part of Labex OSUG@2020. This project received funding from the Shell Game Changer project HiProbe. We acknowledge the European Research Council under grants no. 817803, FAULT-SCAN and no. 742335, F-IMAGE and the European Unions Horizon 2020 research and innovation program under grant agreement No 776622, PACIFIC. The data were provided by NAM (Nederlandse Aardolie Maatschappij). We acknowledge M. Campillo, N. Shapiro, G. Olivier, P. Roux, R. Brossier and C. Voisin for useful discussions. The authors thank Nederlandse Aardolie Maatschappij and Shell for permission to publish. The data are available upon request to NAM (W. Van der Veen).

## REFERENCES

Ben-Zion, Y., Vernon, F. L., Ozakin, Y., Zigone, D., Ross, Z. E., Meng, H., White, M., Reyes, J., Hollis, D., & Barklage, M., 2015. Basic data features and results from a spatially dense seismic array on the San Jacinto fault zone, *Geophysical Journal International*, **202**(1), 370–380.

Boué, P., Poli, P., Campillo, M., Pedersen, H., Briand, X., & Roux, P., 2013. Teleseismic correlations of ambient seismic noise for deep global imaging of the Earth, *Geophysical Journal International*, **194**(2), 844–848.

Bourne, S., Oates, S., & van Elk, J., 2018. The exponential rise of induced seismicity with increasing stress levels in the Groningen gas field and its implications for controlling seismic risk, *Geophysical Journal International*, **213**(3), 1693–1700.

Brenguier, F., Campillo, M., Hadziioannou, C., Shapiro, N., Nadeau, R. M., & Larose, E., 2008a. Post-seismic relaxation along the San Andreas fault at Parkfield from continuous seismological observations, *science*, **321**(5895), 1478–1481.

Brenguier, F., Shapiro, N. M., Campillo, M., Ferrazzini, V., Duputel, Z., Coutant, O., & Nercessian, A., 2008b. Towards forecasting volcanic eruptions using seismic noise, *Nature Geoscience*, **1**(2), 126.

Brenguier, F., Campillo, M., Takeda, T., Aoki, Y., Shapiro, N., Briand, X., Emoto, K., & Miyake, H., 2014. Mapping pressurized volcanic fluids from induced crustal seismic velocity drops, *Science*, **345**(6192), 80–82.

Brenguier, F., Courbis, R., Mordret, A., Campman, X., Boué, P., Chmiel, M., Takano, T., Lecocq, T., Van der Veen, W., Postif, S., & Hollis, D., 2019. Noise-based Ballistic Body-wave Passive Seismic Monitoring, *submitted to Geophysical Journal International*.

Chmiel, M., Mordret, A., Boué, P., Brenguier, F., Lecocq, T., Courbis, R., Hollis, D., Campman, X., Romijn, R., & Van der Veen, W., 2019. Ambient noise multimode Rayleigh and Love wave tomography to determine the shear velocity structure above the Groningen gas field, *Geophysical Journal International*, **218**(3), 1781–1795.

Clements, T. & Denolle, M. A., 2018. Tracking Groundwater Levels using the Ambient Seismic Field, *Geophysical Research Letters*, **45**(13), 6459–6465.

Colombi, A., Chaput, J., Brenguier, F., Hillers, G., Roux, P., & Campillo, M., 2014. On the temporal stability of the coda of ambient noise correlations, *Comptes Rendus Geoscience*, **346**(11), 307–316.

Corciulo, M., Roux, P., Campillo, M., & Dubucq, D., 2012. Instantaneous phase variation for seismic velocity monitoring from ambient noise at the exploration scale, *Geophysics*, **77**(4), Q37–Q44.

de Ridder, S., Biondi, B., & Clapp, R., 2014. Time-lapse seismic noise correlation tomography at Valhall, *Geophysical Research Letters*, **41**(17), 6116–6122.

Donaldson, C., Caudron, C., Green, R. G., Thelen, W. A., & White, R. S., 2017. Relative seismic velocity variations correlate with deformation at Kīlauea volcano, *Science advances*, **3**(6), e1700219.

Durand, S., Montagner, J., Roux, P., Brenguier, F., Nadeau, R., & Ricard, Y., 2011. Passive monitoring of anisotropy change associated with the Parkfield 2004 earthquake, *Geophysical Research Letters*, **38**(13).

Fichtner, A., Kennett, B. L., Igel, H., & Bunge, H.-P., 2008. Theoretical background for continental-and global-scale full-waveform inversion in the time–frequency domain, *Geophysical Journal International*, **175**(2), 665–685.

Fores, B., Champollion, C., Mainsant, G., Albaric, J., & Fort, A., 2018. Monitoring Saturation Changes with Ambient Seismic Noise and Gravimetry in a Karst Environment, *Vadose Zone Journal*, **17**(1).

Froment, B., Campillo, M., Roux, P., Gouedard, P., Verdel, A., & Weaver, R. L., 2010. Estimation of the effect of nonisotropically distributed energy on the apparent arrival time in correlations, *Geophysics*, **75**(5), SA85–SA93.

Gassenmeier, M., Sens-Schönfelder, C., Delatre, M., & Korn, M., 2014. Monitoring of environmental influences on seismic velocity at the geological storage site for CO2 in Ketzin (Germany) with ambient seismic noise, *Geophysical Journal International*, **200**(1), 524–533.

Grinsted, A., Moore, J. C., & Jevrejeva, S., 2004. Application of the cross wavelet transform and wavelet coherence to geophysical time series, *Nonlinear processes in geophysics*, **11**(5/6), 561–566.

Haney, M. M. & Tsai, V. C., 2017. Perturbational and nonperturbational inversion of Rayleigh-wave velocities, *Geophysics*, **82**(3), F15–F28.

Hansen, P. C. & OLeary, D. P., 1993. The use of the L-curve in the regularization of discrete ill-posed problems, *SIAM Journal on Scientific Computing*, **14**(6), 1487–1503.

James, S., Knox, H., Abbott, R., Panning, M., & Screaton, E., 2019. Insights into Permafrost and Seasonal Active-Layer Dynamics from Ambient Seismic Noise Monitoring, *Journal of Geophysical Research: Earth Surface*.

Kimman, W. & Trampert, J., 2010. Approximations in seismic interferometry and their effects on surface waves, *Geophysical Journal International*, **182**(1), 461–476.

KNMI, 2019. KNMI DataCentre, `https://data.knmi.nl/datasets/weer_en_luchtdruk/1.0?q=pressure`, Accessed: 2019-12-02.

Kruiver, P. P., van Dedem, E., Romijn, R., de Lange, G., Korff, M., Stafleu, J., Gunnink, J. L., Rodriguez-Marek, A., Bommer, J. J., van Elk, J., et al., 2017. An integrated shear-wave velocity model for the Groningen gas field, The Netherlands, *Bulletin of Earthquake Engineering*, **15**(9), 3555–3580.

Kumar, P. & Foufoula-Georgiou, E., 1994. Wavelet analysis in geophysics: An introduction, *Wavelets in geophysics*, **4**, 1–43.

Labat, D., 2005. Recent advances in wavelet analyses: Part 1. A review of concepts, *Journal of Hydrology*, **314**(1-4), 275–288.

Larose, E., Carrière, S., Voisin, C., Bottelin, P., Baillet, L., Guéguen, P., Walter, F., Jongmans, D., Guillier, B., Garambois, S., et al., 2015. Environmental seismology: What can we learn on earth surface processes with ambient noise?, *Journal of Applied Geophysics*, **116**, 62–74.

Lecocq, T., Longuevergne, L., Pedersen, H. A., Brenguier, F., & Stammler, K., 2017. Monitoring ground water storage at mesoscale using seismic noise: 30 years of continuous observation and thermo-elastic and hydrological modeling, *Scientific Reports*, **7**(1), 14241.

Lesage, P., Reyes-Dávila, G., & Arámbula-Mendoza, R., 2014. Large tectonic earthquakes induce sharp temporary decreases in seismic velocity in Volcán de Colima, Mexico, *Journal of Geophysical Research: Solid Earth*, **119**(5), 4360–4376.

Mainsant, G., Larose, E., Brönnimann, C., Jongmans, D., Michoud, C., & Jaboyedoff, M., 2012. Ambient seismic noise monitoring of a clay landslide: Toward failure prediction, *Journal of Geophysical Research: Earth Surface*, **117**(F1).

Mao, S., Campillo, M., van der Hilst, R. D., Brenguier, F., Stehly, L., & Hillers, G., 2019a. High temporal resolution monitoring of small variations in crustal strain by dense seismic arrays, *Geophysical Research Letters*, **46**(1), 128–137.

Mao, S., Mordret, A., Campillo, M., Fang, H., & van der Hilst, R. D., 2019b. On the measurement of seismic travel-time changes in the time-frequency domain with wavelet cross-spectrum analysis, *Geophysical Journal International*, ggz495.

Miao, Y., Shi, Y., & Wang, S.-Y., 2018. Temporal change of near-surface shear wave velocity associated with rainfall in Northeast Honshu, Japan, *Earth, Planets and Space*, **70**(1), 204.

Minato, S., Tsuji, T., Ohmi, S., & Matsuoka, T., 2012. Monitoring seismic velocity change caused by the 2011 Tohoku-oki earthquake using ambient noise records, *Geophysical Research Letters*, **39**(9).

Mordret, A., Jolly, A., Duputel, Z., & Fournier, N., 2010. Monitoring of phreatic eruptions using interferometry on retrieved cross-correlation function from ambient seismic noise: Results from Mt. Ruapehu, New Zealand, *Journal of Volcanology and Geothermal Research*, **191**(1-2), 46–59.

Mordret, A., Landès, M., Shapiro, N., Singh, S., & Roux, P., 2014a. Ambient noise surface wave tomography to determine the shallow shear velocity structure at Valhall: depth inversion with a Neighbourhood Algorithm, *Geophysical Journal International*, **198**(3), 1514–1525.

Mordret, A., Shapiro, N. M., & Singh, S., 2014b. Seismic noise-based time-lapse monitoring of the Valhall overburden, *Geophysical Research Letters*, **41**(14), 4945–4952.

Mordret, A., Mikesell, T. D., Harig, C., Lipovsky, B. P., & Prieto, G. A., 2016. Monitoring southwest Greenlands ice sheet melt with ambient seismic noise, *Science advances*, **2**(5), e1501538.

Mordret, A., Sun, H., Prieto, G. A., Toksöz, M. N., & Büyüköztürk, O., 2017. Continuous Monitoring of High-Rise Buildings Using Seismic Interferometry, *Bulletin of the Seismological Society of America*, **107**(6), 2759–2773.

Morlet, J., Arens, G., Fourgeau, E., & Giard, D., 1982a. Wave propagation and sampling theoryPart II: Sampling theory and complex waves, *Geophysics*, **47**(2), 222–236.

Morlet, J., Arens, G., Fourgeau, E., & Glard, D., 1982b. Wave propagation and sampling theoryPart I: Complex signal and scattering in multilayered media, *Geophysics*, **47**(2), 203–221.

Nakata, N. & Snieder, R., 2013. Monitoring a building using deconvolution interferometry. II: Ambient-vibration analysis, *Bulletin of the Seismological Society of America*, **104**(1), 204–213.

Nakata, N., Chang, J. P., Lawrence, J. F., & Boué, P., 2015. Body wave extraction and tomography at Long Beach, California, with ambient-noise interferometry, *Journal of Geophysical Research: Solid Earth*, **120**(2), 1159–1173.

Obermann, A., Planes, T., Larose, E., & Campillo, M., 2013. Imaging preeruptive and coeruptive structural and mechanical changes of a volcano with ambient seismic noise, *Journal of Geophysical Research: Solid Earth*, **118**(12), 6285–6294.

Pacheco, C. & Snieder, R., 2005. Time-lapse travel time change of multiply scattered acoustic waves, *The Journal of the Acoustical Society of America*, **118**(3), 1300–1310.

Planès, T., Mooney, M., Rittgers, J., Parekh, M., Behm, M., & Snieder, R., 2015. Time-lapse monitoring of internal erosion in earthen dams and levees using ambient seismic noise, *Géotechnique*, **66**(4), 301–312.

Pyrak-Nolte, L. J. & Nolte, D. D., 1995. Wavelet analysis of velocity dispersion of elastic interface waves propagating along a fracture, *Geophysical Research Letters*, **22**(11), 1329–1332.

Reasenberg, P. & Aki, K., 1974. A precise, continuous measurement of seismic velocity for monitoring in situ stress, *Journal of Geophysical Research*, **79**(2), 399–406.

Rivet, D., Campillo, M., Shapiro, N. M., Cruz-Atienza, V., Radiguet, M., Cotte, N., & Kostoglodov, V., 2011. Seismic evidence of nonlinear crustal deformation during a large slow slip event in Mexico, *Geophysical Research Letters*, **38**(8).

Rivet, D., Brenguier, F., Clarke, D., Shapiro, N. M., & Peltier, A., 2014. Long-term dynamics of Piton de la Fournaise volcano from 13 years of seismic velocity change measurements and GPS observations, *Journal of Geophysical Research: Solid Earth*, **119**(10), 7654–7666.

Roeloffs, E. A., 1988. Fault stability changes induced beneath a reservoir with cyclic variations in water level, *Journal of Geophysical Research: Solid Earth*, **93**(B3), 2107–2124.

Salvermoser, J., Hadziioannou, C., & Stähler, S. C., 2015. Structural monitoring of a highway bridge using passive noise recordings from street traffic, *The Journal of the Acoustical Society of America*, **138**(6), 3864–3872.

Sens-Schönfelder, C. & Wegler, U., 2006. Passive image interferometry and seasonal variations of seismic velocities at Merapi Volcano, Indonesia, *Geophysical research letters*, **33**(21).

Shapiro, N. M. & Campillo, M., 2004. Emergence of broadband Rayleigh waves from correlations of the ambient seismic noise, *Geophysical Research Letters*, **31**(7).

Snieder, R., Grêt, A., Douma, H., & Scales, J., 2002. Coda wave interferometry for estimating nonlinear behavior in seismic velocity, *Science*, **295**(5563), 2253–2255.

Spica, Z. J., Nakata, N., Liu, X., Campman, X., Tang, Z., & Beroza, G. C., 2018. The ambient seismic field at Groningen gas field: An overview from the surface to reservoir depth, *Seismological Research Letters*, **89**(4), 1450–1466.

Talwani, P., Chen, L., & Gahalaut, K., 2007. Seismogenic permeability, ks, *Journal of Geophysical Research: Solid Earth*, **112**(B7).

Teolis, A. & Benedetto, J. J., 1998. *Computational signal processing with wavelets*, vol. 182, Springer.

TNO, 2019. DINOloket (Internet Portal for Geo-Information), `https://www.dinoloket.nl/en`, Accessed: 2019-09-21.

Toyokuni, G., Takenaka, H., Takagi, R., Kanao, M., Tsuboi, S., Tono, Y., Childs, D., & Zhao, D., 2018. Changes in Greenland ice bed conditions inferred from seismology, *Physics of the Earth and Planetary Interiors*, **277**, 81–98.

van Thienen-Visser, K. & Breunese, J., 2015. Induced seismicity of the Groningen gas field: History and recent developments, *The Leading Edge*, **34**(6), 664–671.

Viens, L., Denolle, M. A., Hirata, N., & Nakagawa, S., 2018. Complex Near-Surface Rheology Inferred From the Response of Greater Tokyo to Strong Ground Motions, *Journal of Geophysical Research: Solid Earth*, **123**(7), 5710–5729.

Voisin, C., Garambois, S., Massey, C., & Brossier, R., 2016. Seismic noise monitoring of the water table in a deep-seated, slow-moving landslide, *SEG Interpretation*, **4**(3), SJ67–SJ76.

Voisin, C., Guzmán, M. A. R., Réfloch, A., Taruselli, M., & Garambois, S., 2017. Groundwater monitoring with passive seismic interferometry, *Journal of Water Resource and Protection*, **9**(12), 1414.

Wapenaar, K., Draganov, D., Snieder, R., Campman, X., & Verdel, A., 2010. Tutorial on seismic interferometry: Part 1Basic principles and applications, *Geophysics*, **75**(5), 75A195–75A209.

Weaver, R. L., Hadziioannou, C., Larose, E., & Campillo, M., 2011. On the precision of noise correlation interferometry, *Geophysical Journal International*, **185**(3), 1384–1392.

Wegler, U. & Sens-Schönfelder, C., 2007. Fault zone monitoring with passive image interferometry, *Geophysical Journal International*, **168**(3), 1029–1033.

Yamamura, K., Sano, O., Utada, H., Takei, Y., Nakao, S., & Fukao, Y., 2003. Long-term observation of in situ seismic velocity and attenuation, *Journal of Geophysical Research: Solid Earth*, **108**(B6).

Yukutake, Y., Ueno, T., & Miyaoka, K., 2016. Determination of temporal changes in seismic velocity caused by volcanic activity in and around Hakone volcano, central Japan, using ambient seismic noise records, *Progress in Earth and Planetary Science*, **3**(1), 29.

Zimmer, M., Prasad, M., & Mavko, G., 2002. Pressure and porosity influences on Vp- Vs ratio in unconsolidated sands, *The Leading Edge*, **21**(2), 178–183.

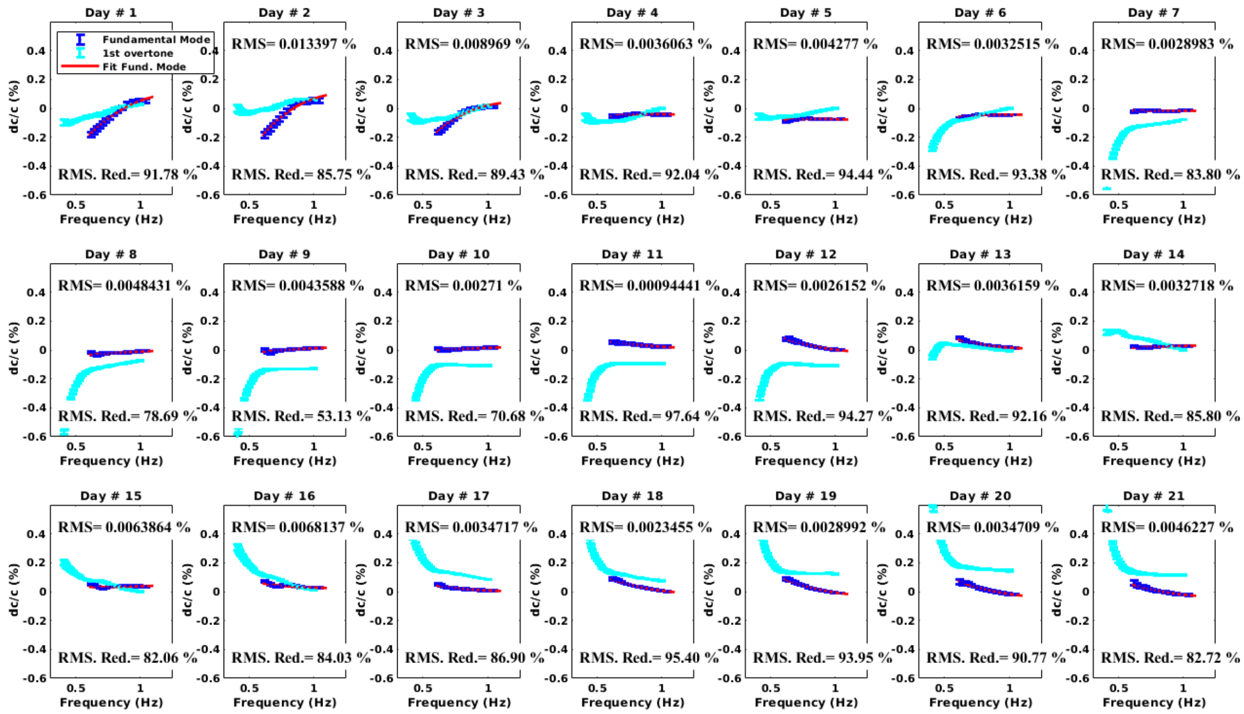


**Figure S1.** Unconstrained inversion: daily differential phase velocity dispersion curves for the fundamental mode (blue curve, the first overtone curve in cyan is shown for reference). The fit to the data after inversion is shown by the inverted dispersion curves in red. The daily misfit value as well as the misfit reduction from $\delta C/C = 0$ are shown in each panel.

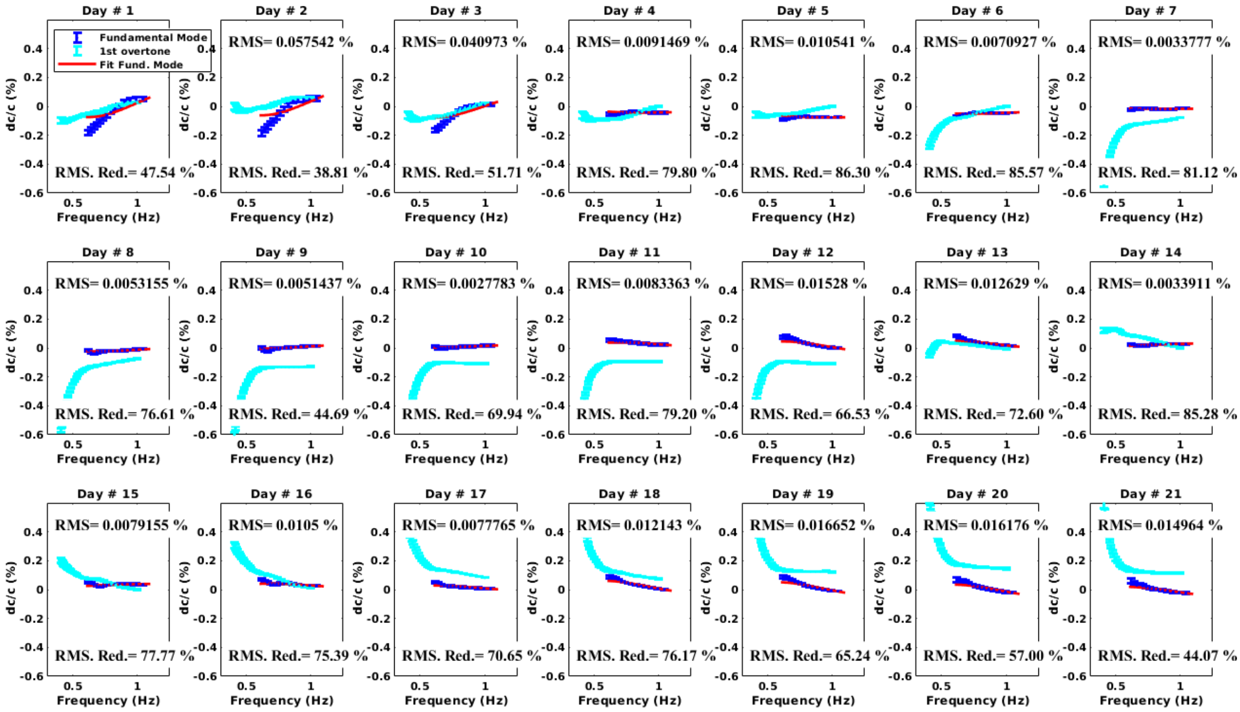


**Figure S2.** Constrained inversion: daily differential phase velocity dispersion curves for the fundamental mode (blue curve, the first overtone curve in cyan is shown for reference). The fit to the data after inversion is shown by the inverted dispersion curves in red. The daily misfit value as well as the misfit reduction from $\delta C/C = 0$ are shown in each panel.

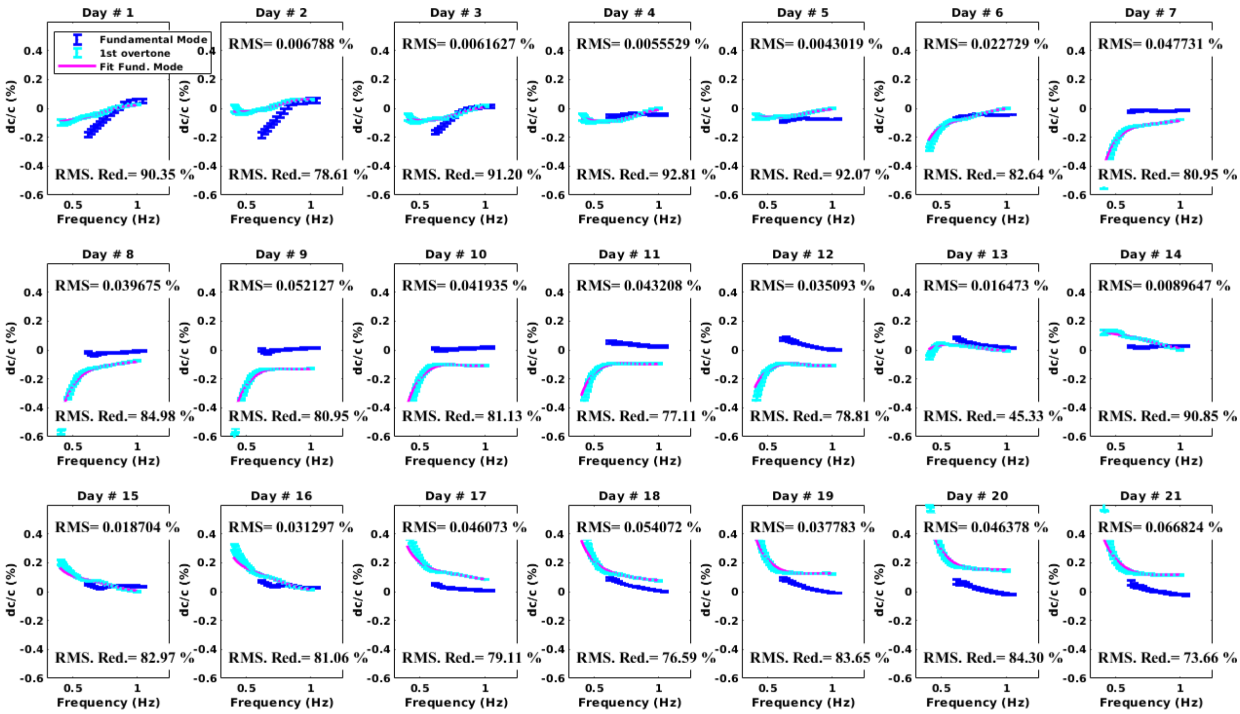


**Figure S3.** Unconstrained inversion: daily differential phase velocity dispersion curves for the full frequency band first overtone (cyan curve, the fundamental mode curve in blue is shown for reference). The fit to the data after inversion is shown by the inverted dispersion curves in magenta. The daily misfit value as well as the misfit reduction from $\delta C/C = 0$ are shown in each panel.

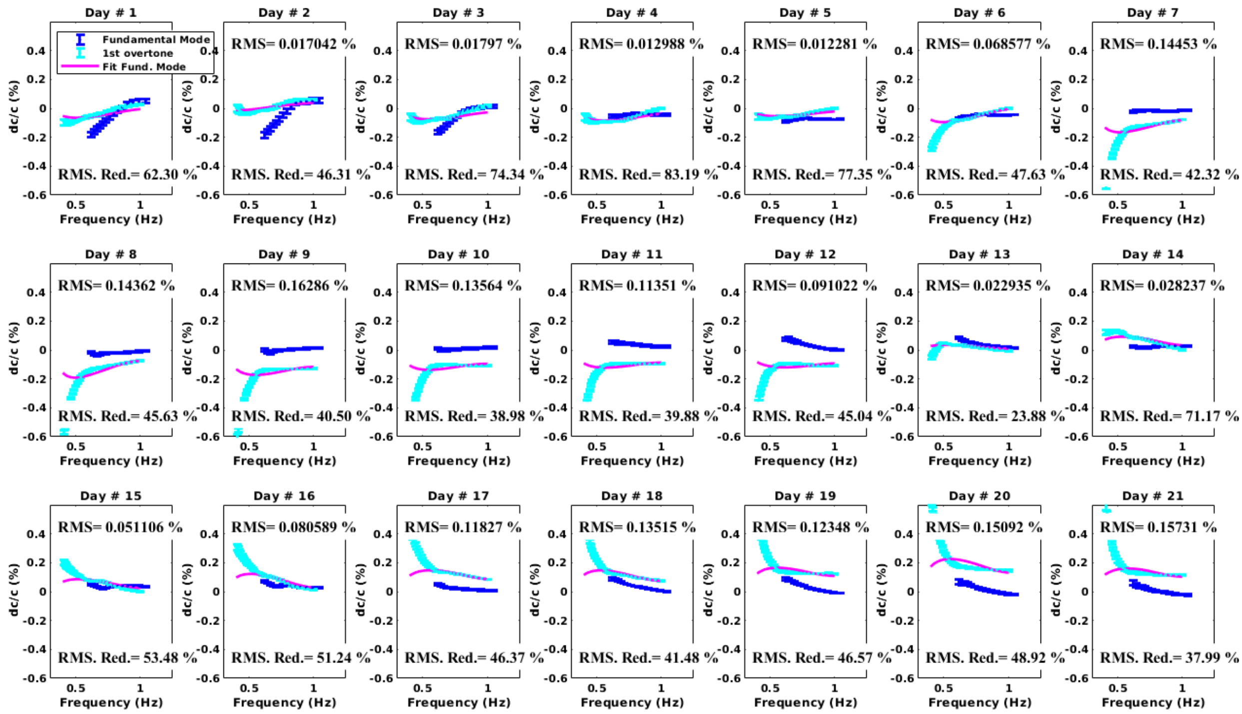


**Figure S4.** Constrained inversion: daily differential phase velocity dispersion curves for the full frequency band first overtone (cyan curve, the fundamental mode curve in blue is shown for reference). The fit to the data after inversion is shown by the inverted dispersion curves in magenta. The daily misfit value as well as the misfit reduction from $\delta C/C = 0$ are shown in each panel.

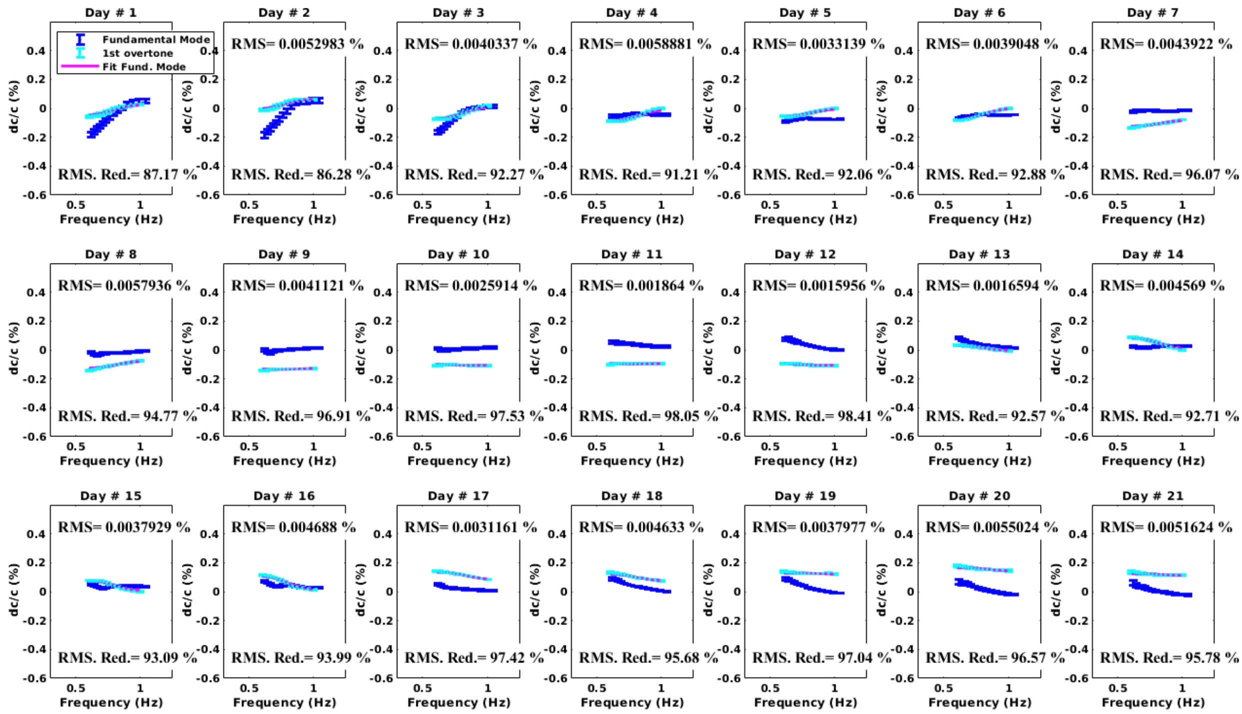


**Figure S5.** Unconstrained inversion: daily differential phase velocity dispersion curves for the first overtone for frequencies $> 0.6$ Hz (cyan curve, the fundamental mode curve in blue is shown for reference). The fit to the data after inversion is shown by the inverted dispersion curves in magenta. The daily misfit value as well as the misfit reduction from $\delta C/C = 0$ are shown in each panel.

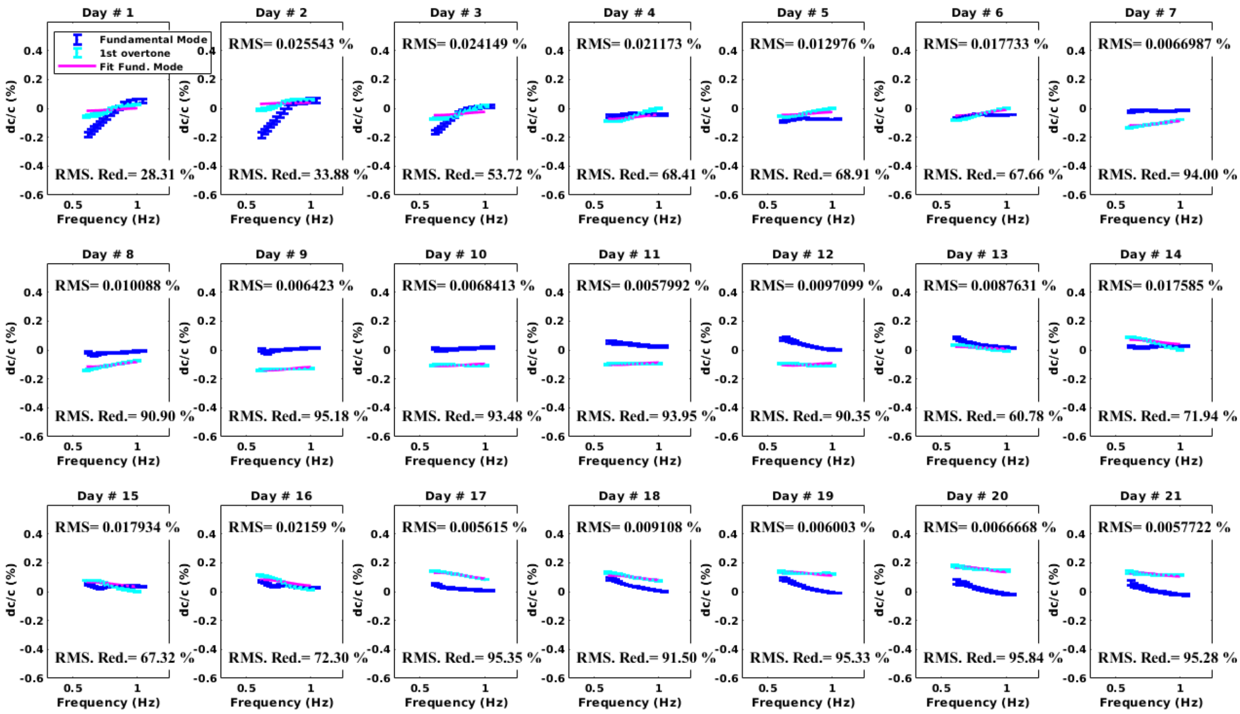


**Figure S6.** Constrained inversion: daily differential phase velocity dispersion curves for the first overtone for frequencies $> 0.6$ Hz (cyan curve, the fundamental mode curve in blue is shown for reference). The fit to the data after inversion is shown by the inverted dispersion curves in magenta. The daily misfit value as well as the misfit reduction from $\delta C/C = 0$ are shown in each panel.

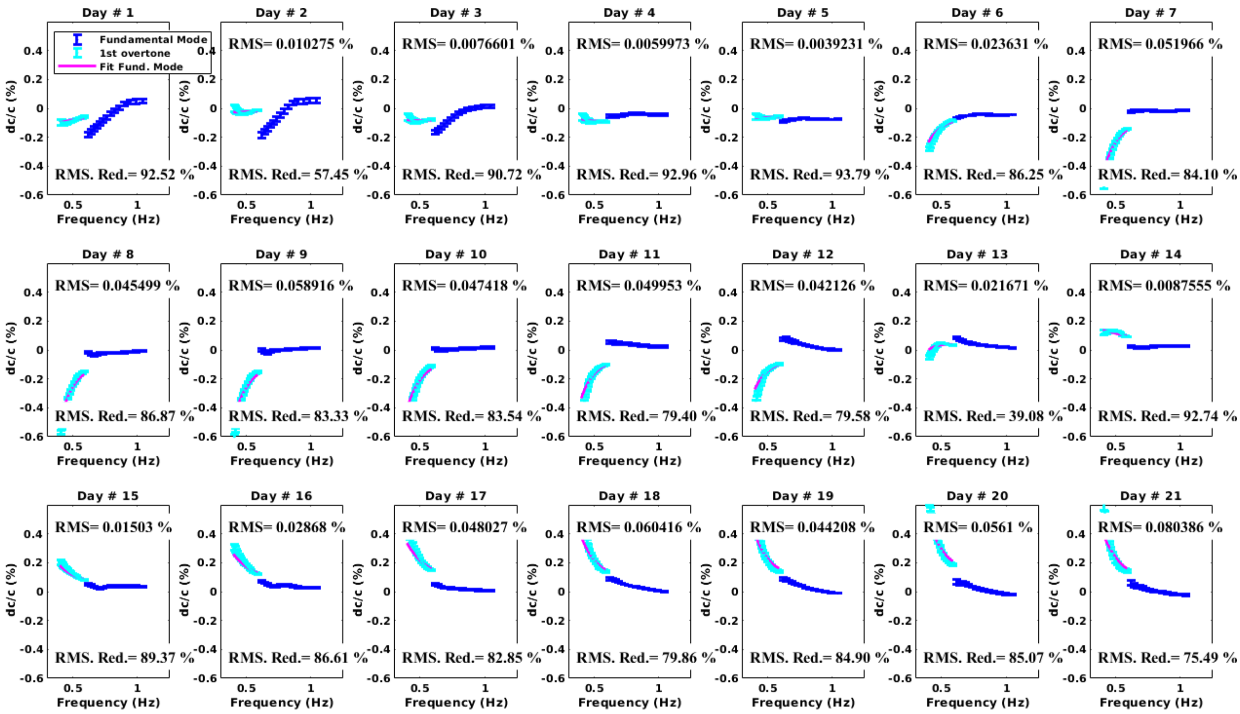


**Figure S7.** Unconstrained inversion: daily differential phase velocity dispersion curves for the first overtone for frequencies $< 0.6$ Hz (cyan curve, the fundamental mode curve in blue is shown for reference). The fit to the data after inversion is shown by the inverted dispersion curves in magenta. The daily misfit value as well as the misfit reduction from $\delta C/C = 0$ are shown in each panel.

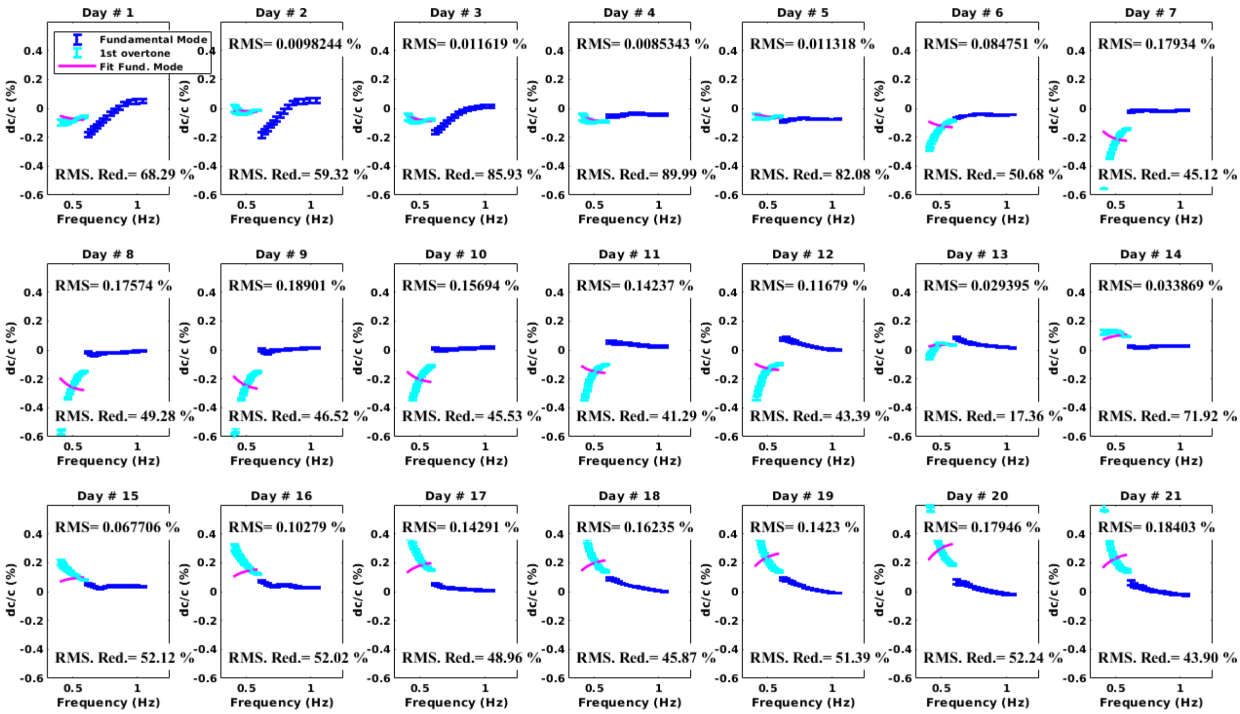


**Figure S8.** Constrained inversion: daily differential phase velocity dispersion curves for the first overtone for frequencies $< 0.6$ Hz (cyan curve, the fundamental mode curve in blue is shown for reference). The fit to the data after inversion is shown by the inverted dispersion curves in magenta. The daily misfit value as well as the misfit reduction from $\delta C/C = 0$ are shown in each panel.